

## Chapter 6: Synthetic clock transitions through continuous dynamical decoupling



Most of the experiments techniques described so far have used the hyperfine  $|m_F\rangle$  states as effective spins and dressed them with an RF or Raman field. However, due to the linear dependence of their energies with respect to magnetic field, and our lack of control of environmental changes we always had to take special care to stabilize the magnetic field in the lab (see Section 3.5.3). An alternative to doing active magnetic field stabilization is to use clock transitions which are first-order insensitive to changes in magnetic field but unfortunately they are not present in all systems or for arbitrary system parameters. However, under almost all circumstances, clock transitions can be synthesized using dynamical decoupling protocols. These protocols involve driving the system with an external oscillatory field, resulting in a dynamically protected ‘dressed’ system.

The idea of implementing continuous dynamical decoupling (CDD) in the lab came from a theoretical proposal to engineer Rashba type SOC using Raman beams and a strong RF field [22], the second being a necessary ingredient for CDD. We initially worked in implementing CDD protocols to create ‘synthetic clock states’ as an intermediate step towards our final goal of engineering Rashba SOC. Just

like with Fourier spectroscopy, CDD became a workhorse of the lab both for the stability it provides against environmental fluctuations and because it has given us access to non-zero matrix coupling elements that we otherwise would not have when working with the bare  $|m_F\rangle$  states. We have continued to use CDD not only for engineering Rashba SOC (Chapter 8) but also to engineer subwavelength optical lattices [23] and Hofstadter [75] cylinders (work in preparation). On the theory side, we developed a proposal that uses them as a platform for emulating  $\mathcal{PT}$  symmetric Hamiltonians [76].

This Chapter discusses the implementation of CDD in the ground  $F = 1$  hyperfine manifold of ultracold  $^{87}\text{Rb}$ . First I give a general overview of dynamical decoupling and continuous dynamical decoupling. Then I describe the technical details and characterization of our CDD protocol which produces a protected three-level system of dressed-states and whose Hamiltonian is fully controllable. Finally, I discuss an implementation of concatenated CDD that renders the system first-order insensitive to both magnetic field noise and noise in the control field. This work was published in [77] and was done in parallel with [78].

## 6.1 Basic principles of CDD

Dynamical decoupling (DD) protocols consist in applying an external control Hamiltonian, generally implemented by a series of pulses, which has the effect of canceling out the dynamics that arise from the quantum system coupling to the environment. DD was first introduced in the context of nuclear magnetic resonance

(NMR) with the discovery of spin-echoes [79], where a single ‘refocusing’ pulse was applied to eliminate dephasing of spins resulting from variations in magnetic field. These ideas were later generalized in [80] to protect a system from decoherence induced by interactions with a quantum environment. Continuous dynamical decoupling (CDD) relies on the application of time-periodic continuous control fields, rather than a series of pulses.

A number of dynamical decoupling protocols, pulsed or continuous, have been shown to isolate quantum systems from low-frequency environmental noise [81–89]. Thus far, CDD has inoculated multi-level systems in nitrogen vacancy centers in diamond, nuclear magnetic resonance experiments, and trapped atomic ions [90–97], from spatiotemporal magnetic field fluctuations.

## 6.2 CDD of a spin-1 system

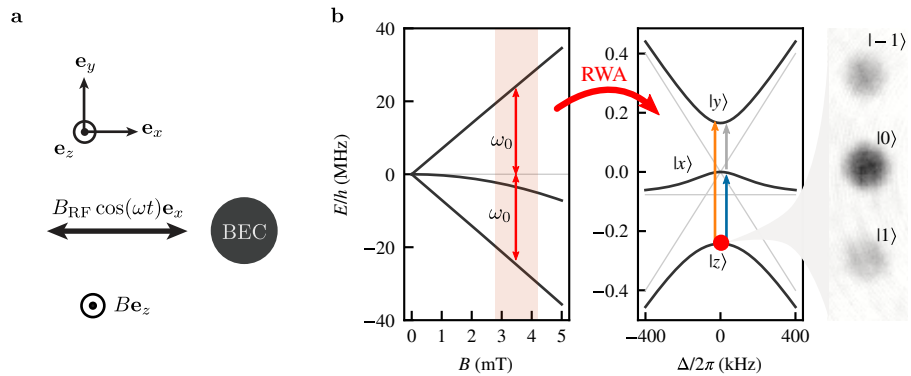


Figure 1: **a.** Setup for implementing CDD using a strong RF magnetic field. **b.** Left: dependence of the  $5^2S_{1/2}$ ,  $F = 1$  ground state of  $^{87}\text{Rb}$  on magnetic field, where the quadratic dependence of the  $|m_F = 0\rangle$  state’s Zeeman shift has been exaggerated so it is visible on the same scale. Center: energies of the  $|xyz\rangle$  eigenstates, for  $\Omega/2\pi = 200$  kHz (black curves) and  $\Omega = 0$  (grey curves). Right: TOF absorption image of  $|z\rangle$  at  $\Delta = 0$ , showing the constituent  $|m_F\rangle$  states.

We implemented CDD using a strong RF magnetic field with strength  $\Omega$  which linked the three  $|m_F\rangle$  states comprising the  $F = 1$  electronic ground state manifold of  $^{87}\text{Rb}$ . The RF field was linearly polarized along  $\mathbf{e}_x$ , and had angular frequency  $\omega$  close to the Larmor frequency  $\omega_0 = g_F\mu_B B_0$  from a magnetic field  $B_0\mathbf{e}_z$ ;  $g_F$  is the Lande  $g$ -factor and  $\mu_B$  is the Bohr magneton. Using the rotating frame approximation for the frame rotating at  $\omega$  (which is valid for  $\omega \gg \Omega$ ), the system is described by

$$\hat{H} = \hbar\Delta\hat{F}_z + \hbar\epsilon(\hat{F}_z^2 - \hat{\mathbb{1}}) + \hbar\Omega\hat{F}_x, \quad (6.1)$$

with detuning  $\Delta = \omega - \omega_0$ , quadratic Zeeman shift  $\epsilon$ , spin-1 angular momentum operators  $\hat{F}_{x,y,z}$ , and the identity operator  $\hat{\mathbb{1}}$ .

### 6.3 The $|xyz\rangle$ states

The eigenstates of Equation 6.1 correspond to the CDD basis. In this section, I describe their properties and show that their energies are first-order insensitive to magnetic field fluctuations.

#### 6.3.1 State decomposition

We denote the eigenstates of Equation 6.1 by  $|x\rangle$ ,  $|y\rangle$  and  $|z\rangle$ . The CDD states are linear combinations of the  $|m_F\rangle$  basis states, and for  $\Delta = 0$  the (non-normalized)

eigenvectors are:

$$\begin{aligned}
|x\rangle &= | -1 \rangle - | 1 \rangle, \\
|y\rangle &= | -1 \rangle - \frac{\epsilon + \tilde{\Omega}}{\sqrt{2\Omega}} | 0 \rangle + | 1 \rangle, \\
|z\rangle &= | -1 \rangle - \frac{\epsilon - \tilde{\Omega}}{\sqrt{2\Omega}} | 0 \rangle + | 1 \rangle.
\end{aligned} \tag{6.2}$$

Figure 2 shows the normalized full state decomposition as a function of  $\Delta$ , where it can be seen that the  $|xyz\rangle$  states adiabatically map to the  $|m_F\rangle$  states for  $|\Delta| \gg \Omega$ : for positive (negative) detuning  $|z\rangle$  maps to  $|1\rangle$  ( $| -1 \rangle$ );  $|y\rangle$  maps in the exact opposite way to  $|z\rangle$ ; and  $|x\rangle$  always maps to  $|0\rangle$ .

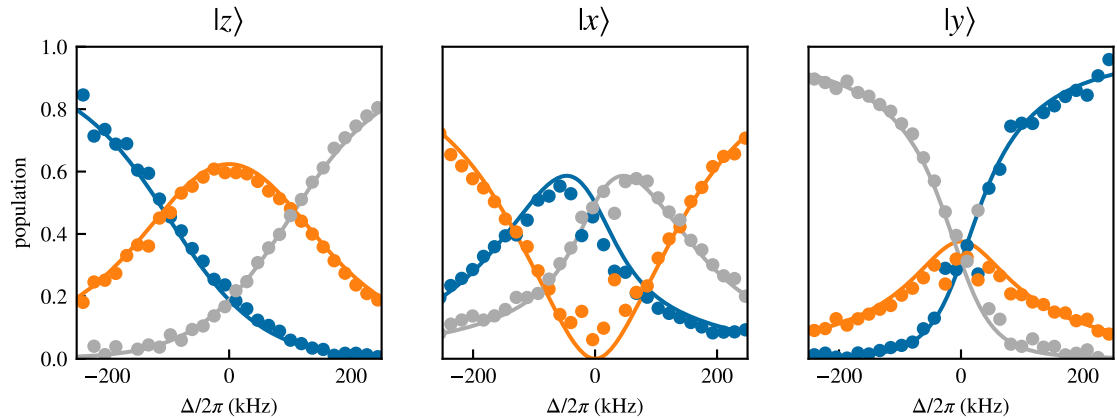


Figure 2: Decomposition of the  $|xyz\rangle$  states on the  $|m_F\rangle$  basis for  $\Omega/2\pi = 145(1)$  kHz. The  $|m_F = -1, 0, 1\rangle$  states correspond to blue, orange, gray respectively.

We labeled our dressed states  $|xyz\rangle$  since for  $\Omega \rightarrow 0^+$  and  $\Delta = 0$ , they contin-

uously approach the  $|XYZ\rangle$  states familiar from quantum chemistry [18]:

$$\begin{aligned} |X\rangle &= \frac{|1\rangle - |-1\rangle}{\sqrt{2}}, \\ |Y\rangle &= i\frac{|1\rangle + |-1\rangle}{\sqrt{2}}, \\ |Z\rangle &= |0\rangle. \end{aligned} \tag{6.3}$$

which transform under the application of the spin-1 operators as  $\epsilon_{jkl}\hat{F}_j|k\rangle = i\hbar|l\rangle$ , so that a resonant probe field can induce transitions between at least one pair of states, irrespectively of its polarization.

Finally, when  $\Omega \rightarrow \infty$  they are independent of the driving field amplitude and continuously approach the eigenstates of the  $\hat{F}_x$  operator

$$\begin{aligned} |x\rangle &= |1\rangle - |-1\rangle, \\ |y\rangle &= |1\rangle + \sqrt{2}|0\rangle + |-1\rangle, \\ |z\rangle &= |1\rangle - \sqrt{2}|0\rangle + |-1\rangle. \end{aligned} \tag{6.4}$$

### 6.3.2 Energies

The clock-like nature of these states is determined by their eigenvalues which are even functions with respect to  $\Delta$  as can be seen by the leading order expansion

of the eigenenergies  $E_i = \hbar\omega_i$  for  $\Delta \rightarrow 0$

$$\begin{aligned}\omega_x &= -\frac{\epsilon}{\Omega^2}\Delta^2 + \mathcal{O}(\Delta^4), \\ \omega_y &= \frac{1}{2}(-\epsilon + \tilde{\Omega}) - \frac{(\epsilon + \tilde{\Omega})}{-\epsilon^2 - 4\Omega^2 + \epsilon\tilde{\Omega}}\Delta^2 + \mathcal{O}(\Delta^4), \\ \omega_z &= \frac{1}{2}(-\epsilon - \tilde{\Omega}) + \frac{(\epsilon - \tilde{\Omega})}{\epsilon^2 + 4\Omega^2 + \epsilon\tilde{\Omega}}\Delta^2,\end{aligned}\tag{6.5}$$

where we have defined  $\tilde{\Omega} = \sqrt{4\Omega^2 + \epsilon^2}$ . The energy differences  $\hbar\omega_{xy}$ ,  $\hbar\omega_{zy}$  and  $\hbar\omega_{zx}$  are only quadratically sensitive to  $\Delta$  for  $\Delta \ll \Omega$ <sup>1</sup> so that detuning fluctuations  $\delta\Delta$  are suppressed to first order, making these a trio of synthetic clock states. The curvatures of  $\omega_x$  and  $\omega_z$  have the same sign and in principle there is a critical value of  $\Omega$  where the quadratic term in transition energy can be made arbitrarily small, making it quartic in  $\Delta$ . However, this cancellation does not take place when we consider the dependence of  $\epsilon$  on  $\Delta$  from the Breit-Rabi expression. It is still possible to find an optimal  $\Omega$  for which  $\omega_{zx}$  depends quartically on  $\Delta$ , but it does not occur at  $\Delta = 0$  as is predicted by Equation 6.5 for constant  $\epsilon$ .

### 6.3.3 Transition matrix elements

Unlike the  $|m_F\rangle$  basis, an oscillatory magnetic field with the right polarization can drive transitions between all pairs of the  $|xyz\rangle$  states with non-zero transition matrix elements. The transition matrix elements between the  $|xyz\rangle$  have a dependence on both  $\Omega$  and  $\Delta$ . For the  $\Delta = 0$  case they can be read from the representation of the spin-1 matrices in the  $|xyz\rangle$  basis

---

<sup>1</sup>The energies are quadratic in  $\Delta$  for  $\Delta \ll \Omega$ , and linear for  $\Delta \gg \Omega$  with a slope of 7 MHz/mT.

$$\begin{aligned}
\hat{F}_x &\rightarrow \begin{pmatrix} \frac{2\Omega}{\tilde{\Omega}} & 0 & -\frac{\epsilon}{\tilde{\Omega}} \\ 0 & 0 & 0 \\ -\frac{\epsilon}{\tilde{\Omega}} & 0 & -\frac{2\Omega}{\tilde{\Omega}} \end{pmatrix} \\
\hat{F}_y &\rightarrow \begin{pmatrix} 0 & -\frac{i(\tilde{\Omega}-\epsilon)}{\Omega\sqrt{\frac{(\epsilon-\tilde{\Omega})^2}{\Omega^2}+4}} & 0 \\ \frac{i(\tilde{\Omega}-\epsilon)}{\Omega\sqrt{\frac{(\epsilon-\tilde{\Omega})^2}{\Omega^2}+4}} & 0 & -\frac{i(\tilde{\Omega}+\epsilon)}{\Omega\sqrt{\frac{(\tilde{\Omega}+\epsilon)^2}{\Omega^2}+4}} \\ 0 & \frac{i(\tilde{\Omega}+\epsilon)}{\Omega\sqrt{\frac{(\tilde{\Omega}+\epsilon)^2}{\Omega^2}+4}} & 0 \end{pmatrix} \\
\hat{F}_z &\rightarrow \begin{pmatrix} 0 & -\frac{\sqrt{\frac{\epsilon}{\tilde{\Omega}}+1}}{\sqrt{2}} & 0 \\ -\frac{\sqrt{\frac{\epsilon}{\tilde{\Omega}}+1}}{\sqrt{2}} & 0 & -\frac{2}{\sqrt{\frac{(\tilde{\Omega}+\epsilon)^2}{\Omega^2}+4}} \\ 0 & -\frac{2}{\sqrt{\frac{(\tilde{\Omega}+\epsilon)^2}{\Omega^2}+4}} & 0 \end{pmatrix}, \tag{6.6}
\end{aligned}$$

where the states have been ordered by decreasing energy ( $|y\rangle$ ,  $|x\rangle$ ,  $|z\rangle$ ). We therefore see that a term in a Hamiltonian that is proportional to  $\hat{F}_x$  can only drive transitions between  $|z\rangle$  and  $|y\rangle$  and that a coupling term proportional to  $\hat{F}_y$  and  $\hat{F}_z$  can drive both drive transitions between  $|z\rangle$  and  $|x\rangle$  or  $|x\rangle$  and  $|y\rangle$  with different strengths. It can be seen from Equation 6.6 that when  $\Omega$  and  $\epsilon$  are comparable in magnitude there exists at least one non-zero transition matrix element for each pair of dressed states and they can all be coupled cyclically.

## 6.4 $|xyz\rangle$ state preparation

We implemented CCD to BECs with  $N \approx 5 \times 10^4$  atoms. For all of the experiments described in this Chapter the dipole trap had trapping frequencies of  $(f_x, f_y, f_z) = (42(3), 34(2), 133(3))$  Hz. We applied a  $B_0 \approx 3.27$  mT bias field that lifted the ground state degeneracy, giving an  $\omega_0/2\pi = 22.9$  MHz Larmor frequency, with a quadratic shift  $\epsilon/2\pi = 76.4$  kHz. We determined that the ambient magnetic field fluctuations were dominated by contributions from line noise giving an RMS uncertainty  $\delta\Delta/2\pi = g_F\mu_B\delta B/h = 0.67(3)$  kHz.

The state preparation consisted of two stages of ARP. On the first stage we followed the usual protocol described in Section 3.5.2 to prepare the BEC in any of the  $|m_F = 0, -1, 1\rangle$  states. On the second stage, we adiabatically transformed the  $|m_F\rangle$  states into the  $|xyz\rangle$  states. We started with the bias field far from resonance ( $\Delta(t = 0)/2\pi \approx -450$  kHz) and with all coupling fields off. Then we ramped on  $\Omega$  in a two-step process. We first ramped from  $\Omega = 0$  to an intermediate value  $\Omega_{\text{mid}}$ , approximately half its final value in 1 ms. We then ramped  $\Delta$  to zero in 3 ms by increasing the magnetic field  $B_0$ . After allowing  $B_0$  to stabilize for 30 ms, we ramped the RF dressing field to its final value  $\Omega$  in 1 ms, yielding the dynamically decoupled  $|xyz\rangle$  states. It was important that we waited for the field to stabilize at an intermediate  $\Omega_{\text{mid}}$  as we found several times that the capacitors on the impedance matching network of the antenna used to generate the RF field would burn if we kept the power on for too long.

After performing any experiment with the  $|xyz\rangle$  states we measured their pop-

ulations by adiabatically deloading them back into the  $|m_F\rangle$  basis. We first ramped  $B_0$  so that  $\Delta$  approached its initial detuned value in 2 ms, and then ramped off the dressing RF field in 1 ms. A typical experimental sequence for  $\Delta$  and  $\Omega$  can be visualized in Figure 4. As usual, we obtained the spin-resolved momentum distribution using absorption imaging after TOF, with a Stern-Gerlach field to spatially separate the spin components. The right panel of Figure 1b shows a TOF image of the  $|m_F\rangle$  state decomposition of the  $|z\rangle$  state. For this image as well as for the measurement of the dressed state decomposition shown in Figure 2 we suddenly (not-adiabatically) turned the RF coupling off, thereby projecting the  $|xyz\rangle$  states back into the  $|m_F\rangle$  basis.

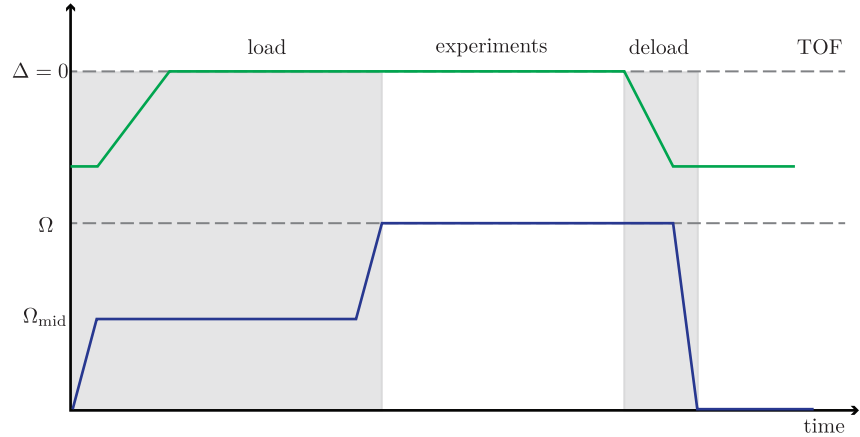


Figure 3: Detuning and RF coupling strengths ramps (not to scale) performed to adiabatically prepare the  $|xyz\rangle$  states starting in the  $|m_F\rangle$  states and vice versa.

## 6.5 Initial characterization of $\Omega$

Producing RF fields with large coupling strength was not a trivial task and when testing different antenna designs it was important to have an easy and quick

way of characterizing them. We mostly relied on two different techniques to get an initial estimate of  $\Omega$ : first, we prepared atoms in  $|m_F = -1\rangle$  and pulse on the RF to drive transitions between the three  $|m_F\rangle$  states. We would then fit the populations in the three states as a function of pulsing time to the time evolution given the time dependent Schrödinger equation for the RF Hamiltonian (Equation 6.1) with  $\Omega$  and  $\Delta$  as free parameters.

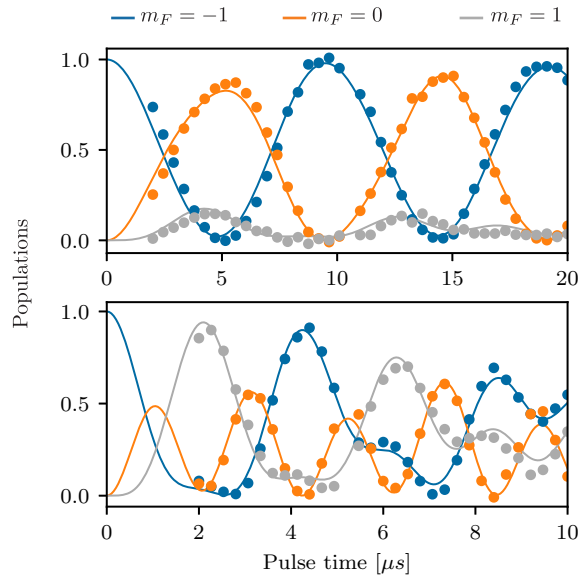


Figure 4: We prepared the system in the  $|m_F = -1\rangle$  state and pulsed  $\Omega$  for variable times. We fit the populations in the  $|m_F\rangle$  states as a function of pulsing time to get an initial estimate of  $\Omega$ . The top panel shows the time evolution of  $\Omega/2\pi \approx 76$  kHz and the bottom panel shows the evolution for  $\Omega/2\pi \approx 238$  kHz

Alternatively, we followed the loading procedure described in [Section 6.4](#) but suddenly turned  $\Omega$  off for different values of  $\Delta$  to get the decomposition of the  $|xyz\rangle$  states in terms of the  $|m_F\rangle$  states. We then fit the populations to the eigenstates of the Equation 6.1 with  $\Omega$  and  $\Delta$  as free parameters. Figure 2 is an example of such type of calibration.

For an antenna with a [high](#) quality factor such as ours ( $q \sim 20$ ) we could not

‘suddenly’ turn  $\Omega$  on or off as it takes some time for power to build up and to die out when the RF fields are turned on or off. If we did not include this into the model used to calibrate  $\Omega$  we could get some results that were slightly off. We only used these measurements as initial estimates and once we found an antenna design that could produce a large enough  $\Omega$  we used the spectroscopy techniques described in the next section to fully characterize the system.

## 6.6 Spectroscopy

We confirmed our control and measurement techniques spectroscopically by measuring the energy differences between the  $|xyz\rangle$  states with an additional probing field with angular frequency  $\omega + \omega_p$ , coupling strength  $\Omega_p$  and polarized along  $\mathbf{e}_y$ . In the frame rotating with angular frequency  $\omega$  and after using a RWA the system was described by the Hamiltonian

$$\begin{aligned}\hat{H} = & \Delta\hat{F}_z + \hbar\epsilon(\hat{F}_z^2/\hbar^2 - \hat{\mathbb{I}}) + \Omega\hat{F}_x \\ & + \Omega_p (\sin(\omega_p t)\hat{F}_x + \cos(\omega_p t)\hat{F}_y).\end{aligned}\quad (6.7)$$

In this rotating frame the probe field initially polarized along  $\mathbf{e}_y$  has components along  $\mathbf{e}_x$  and  $\mathbf{e}_y$ , resulting in at least one non-zero transition matrix element for all transitions between pairs of dressed states. If the probing field was polarized along  $\mathbf{e}_z$  we would not be able to drive the  $zy$  transition as can be seen from the matrix elements in Equation 6.6.

To probe the dependence of the  $|xyz\rangle$  state energies on detuning, we performed

Rabi spectroscopy (Section 3.5.1) by pulsing  $\Omega_p$  on for a constant time and scanned  $\omega_p$  for different values of  $\Delta$ . Figure 1b shows the spectroscopically resolved values of  $\omega_{xy}/2\pi$ ,  $\omega_{yz}/2\pi$ , and  $\omega_{zx}/2\pi$  for  $\Omega/2\pi = 194.5(1)$  kHz and the side panel shows a sample spectra measured with coupling strength  $\Omega_p/2\pi \approx 1$  kHz and  $\Delta/2\pi \approx 9$  kHz. The dashed curves were computed by diagonalizing Equation 6.1, and they clearly depart from our measurements for the  $zx$  transition. This departure results from neglecting the weak dependence of the quadratic shift  $\epsilon$  on bias field  $B_0$ . In near-perfect agreement with experiment, the solid curves from the full Breit-Rabi expression account for this dependency.

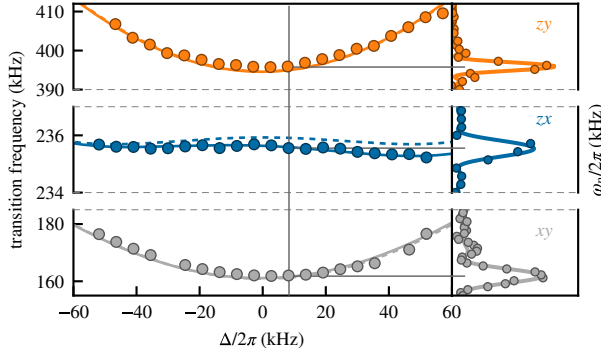


Figure 5: Left: spectroscopic data showing transitions between the  $|xyz\rangle$  states for  $\Omega/2\pi = 194.5(1)$  kHz. The vertical scale of the center panel ( $zx$  transition) has only 10% the range of the other panels. The dashed lines correspond to the Hamiltonian of Equation 6.1 while the solid lines include the dependence of the quadratic shift on  $\Delta$ . Right: representative spectra.

## 6.7 Robustness

We focus on the robustness of the  $zx$  transition which can be made virtually independent of magnetic field variations due to the similar curvature of  $\omega_z(\Delta)$  and  $\omega_x(\Delta)$  (see the middle panel of Figure 1b). We quantified the sensitivity of this trans-

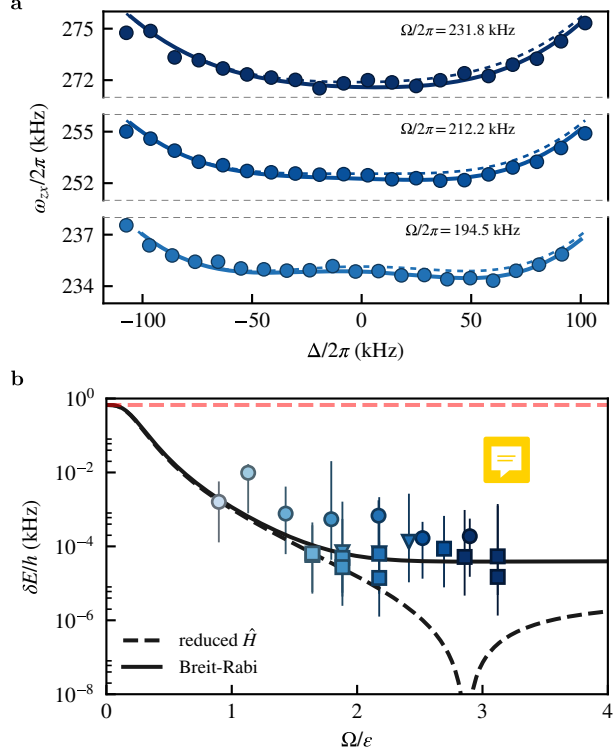


Figure 6: **a.** Transition frequency  $\omega_{zx}/2\pi$  for three values of  $\Omega/2\pi$ . The dashed curves correspond to Equation 6.7, while the solid curves use the Breit-Rabi expression. **b.** The change in energy from our experimental detuning fluctuations as measured in the  $|m_F\rangle$  basis is  $\delta\Delta/2\pi = 0.67$  kHz (red dashed line). Triangles correspond to  $|xyz\rangle$  spectroscopy data, squares to side-of-peak  $\pi$ -pulse data, and circles to double-dressed data. The black dashed (solid) curve was calculated using Equation 6.7 (the Breit-Rabi expression). The shading of the data points corresponds to the Rabi frequencies in Figure 8.

sition to field variations with three methods corresponding to the different markers in Figure 6b: (1) Triangles denote data using Rabi spectroscopy as in Figure 6a. (2) Squares denote data in which a detuned  $\pi$ -pulse of the probe field transferred approximately half of the atoms from  $|z\rangle$  to  $|x\rangle$ . This ‘side-of-peak’ technique overcomes the limitation of Rabi spectroscopy being first-order insensitive to changes in  $\omega_{zx}$ . (3) Circles describe data using a double dressing technique that will be described in Section 6.9. In each case we measured the energy shift from resonance as

a function of detuning (magnetic field) and then used a fourth-order polynomial fit to extract the RMS residuals  $\delta\omega_{zx}$  due to the known detuning noise <sup>2</sup>. The results are not consistent with the ~~theory simple~~ from Equation 6.7 (dashed) and instead require the Breit-Rabi expression (solid) to obtain full agreement <sup>3</sup>.

Even at our smallest coupling  $\Omega/2\pi = 69(1)$  kHz the typical magnetic field noise was attenuated by two orders of magnitude, rendering it essentially undetectable. Ideally, the radius of curvature of  $\omega_{zx}(\Delta)$  changes sign at about  $\Omega/2\pi = 220$  kHz, leaving only a  $\Delta^4$  contribution, however, in practice the small dependence of  $\epsilon$  on  $B$  prevents this perfect cancellation. Still it is possible to see the changing curvature of  $\omega_{zx}(\Delta)$  near  $\Delta = 0$  for different values of  $\Omega$  in Figure 6a.

### 6.7.1 Optimal response to noise

The sensitivity of the  $zx$  transition to detuning fluctuations can be optimized further by working at  $\Delta \neq 0$  as shown in Figure 7.

For small values of  $\Omega$ , the optimum value of  $\Delta$  corresponds to one of the concave features of the  $zx$  transition energy that arises due to the asymmetry introduced by the quadratic shift. As  $\Omega$  gets larger, these features merge into a single one and the optimum value is  $\Delta \approx 0$ . The deviation from  $\Delta = 0$  is due to an overall tilt of the transition energy coming from the dependence of the quadratic shift on  $\Delta$ . At the optimum point  $\Omega/\epsilon \approx 3$  the sensitivity of the synthetic clock transition

---

<sup>2</sup>Our procedure also quantifies the small fluctuations that survive for spectra that are flat beyond second order, as in Equation 6.1.

<sup>3</sup>The fluctuations can be even smaller for a given  $\Omega$  if we allow for  $\Delta \neq 0$ .

is  $1.9 \times 10^{-7}$  kHz, c.f, the  $^{87}\text{Rb}$  clock transition which scales as  $57.5$  kHz/mT<sup>2</sup> and gives  $5.8 \times 10^{-7}$  kHz.

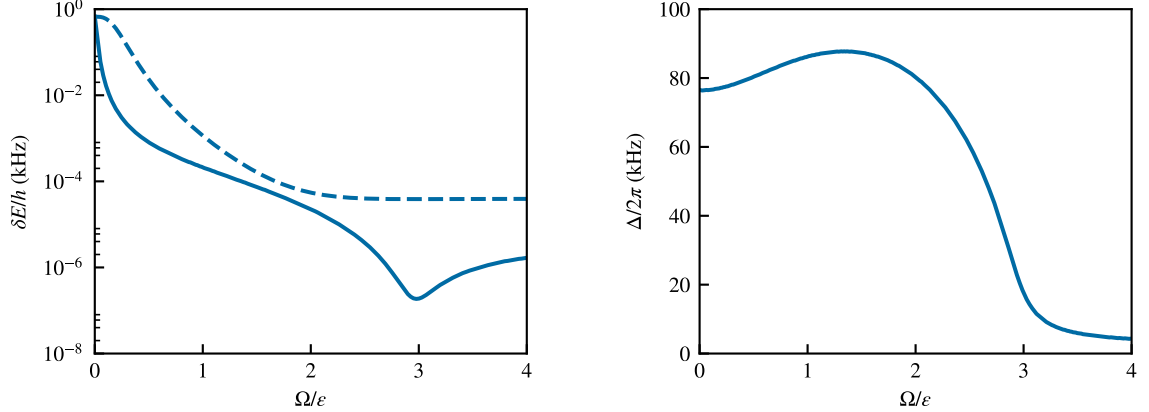


Figure 7: Left: Optimum response (solid) of the  $zx$  transition to detuning fluctuations allowing for finite  $\Delta$  compared to  $\Delta = 0$  (dashed) for the full Breit-Rabi model. Right: The values of  $\Delta$  that correspond to the minimum derivative of  $\omega_{zx}$ .

## 6.8 Driving dressed state transitions

We explored the strength of the probe-driven transitions between these states by observing coherent Rabi oscillations (Figure 8a) where our BEC was prepared in  $|z\rangle$  and the probe field had strength  $\Omega_p/2\pi \approx 1$  kHz. The top panel shows Rabi oscillations between  $|m_F = 0\rangle$  and  $|m_F = -1\rangle$  states for reference, and the remaining panels show oscillations between  $|z\rangle$  and  $|x\rangle$ . The observed Rabi frequency between dressed states decreased with increasing  $\Omega$  indicating a dependence of the  $zx$  transition matrix elements on  $\Omega$ . We repeated this experiment driving all possible pairs of dressed state transitions at fixed  $\Omega_p$  for, and Figure 8b shows the dependence of these matrix elements on  $\Omega$  for  $\Delta = 0$ .

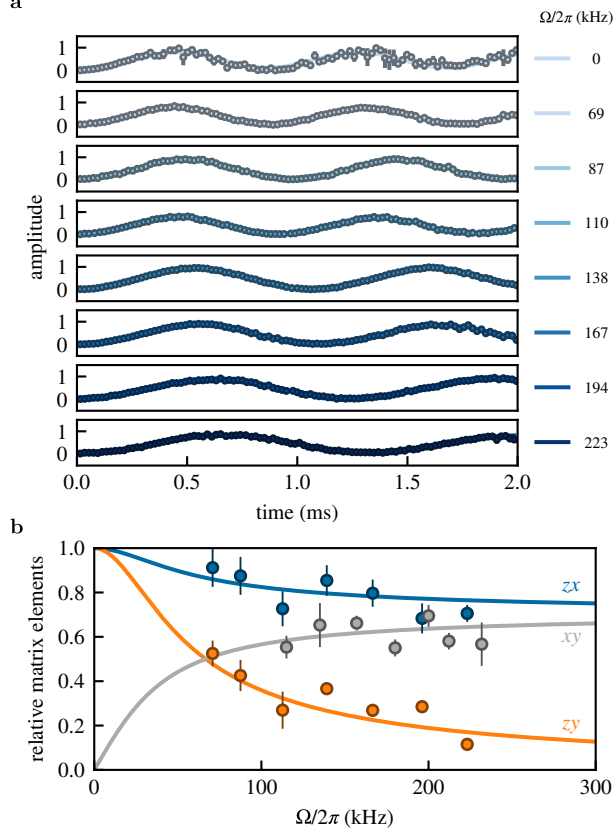


Figure 8: **a.** Rabi oscillations. Phase coherence is maintained throughout the oscillations in the dressed basis, while it is quickly lost in the  $|m_F\rangle$  basis. The marker size reflects the typical uncertainties on the dressed basis oscillations. **b.** Transition matrix elements for  $zx$  (blue) and  $zy$  (orange) transitions decrease monotonically with increasing  $\Omega$  for  $\Delta = 0$ , while they increase for  $xy$ .

The coherence of the Rabi oscillations for longer times was limited by gradients in  $\Omega$  that lead to phase separation of the dressed states, and therefore loss of contrast in the oscillations. This effect was faster for smaller frequency Rabi oscillations. For example for  $\Omega_p/2\pi = 5$  kHz we observed coherent Rabi oscillations with almost full contrast for more than 10 ms while for the  $\Omega_p/2\pi = 870$  Hz oscillation shown in Figure 9 the contrast was significantly reduced after 5 ms. The loss of contrast was even worse when we tried performing a Ramsey sequence where the time evolution is most sensitive to the environment. One solution to this problem would be to change

the experimental setup to a double loop antenna to generate a more spatially uniform magnetic field.

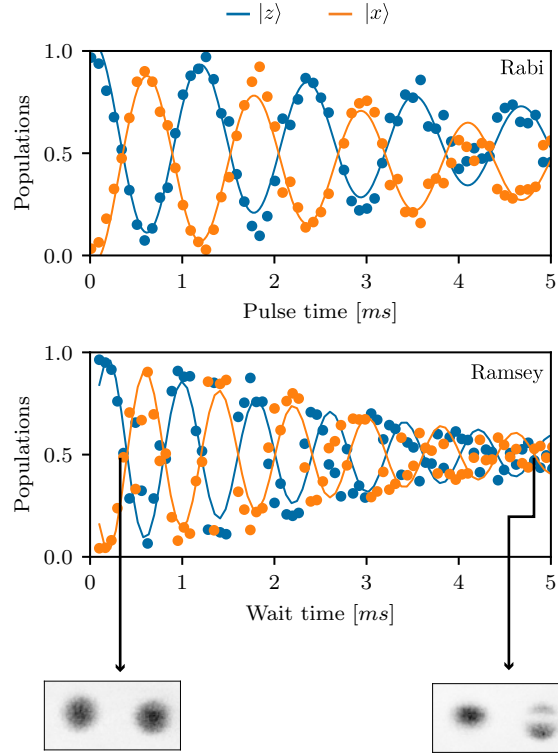


Figure 9: Loss of contrast in coherent oscillations. A Rabi oscillation (top) between the  $|z\rangle$  and  $|x\rangle$  states with  $\Omega_p/2\pi = 870$  Hz decays by  $1/e$  in 4.6 ms and a Ramsey oscillation (middle) with about 1 kHz frequency decays in about 3 ms. The gradients in  $\Omega$  lead to phase separation of dressed states and loss of contrast for longer pulse/wait times.

In comparison, we found that for both Rabi and Ramsey oscillations between the  $|m_F\rangle$  states the phase started deteriorating after a few hundreds of  $\mu$ s, this is not surprising due to bias magnetic field temporal noise. We canceled gradient magnetic fields so that no phase separation of the bare states was observed for  $> 10$  sec. As a result, the system can in principle undergo coherent evolution without loss of contrast for a long time but because of field fluctuations between shots what we observed instead was full contrast noise.

## 6.9 Concatenated CDD

The driving field  $\Omega$  coupled together the  $|m_F\rangle$  states, giving us the  $|xyz\rangle$  synthetic clock states that were first-order insensitive to magnetic field fluctuations. However, the spectrum of these states is still first-order sensitive to fluctuations of the driving field  $\delta\Omega$ . Reference [85] showed that an additional field coupling together with these  $|xyz\rangle$  states can produce doubly-dressed states that are insensitive to both  $\delta\Omega$  and  $\delta\Delta$ : a process called concatenated CDD. In our experiment, the probe field provided the concatenating coupling field. Because  $\Omega_p \ll \Omega$ , we focus on a near-resonant two-level system formed by a single pair of dressed states, here  $|z\rangle$  and  $|x\rangle$ , which we consider as pseudospins  $|\uparrow\rangle$  and  $|\downarrow\rangle$ . These states are described by the effective two-level Hamiltonian

$$\hat{H}_p = \frac{\hbar\Delta'}{2}\hat{\sigma}_3 + \hbar\Omega' \cos(\omega_p t)\hat{\sigma}_1, \quad (6.8)$$

with energy gap  $\Delta' \approx \omega_{z,x}$  (shifted by off-resonant coupling to the  $zy$  and  $xy$  transitions) and coupling strength  $\Omega' \propto \Omega_p$ , as set by the matrix elements displayed in Figure 8b. Here  $\hat{\sigma}_{1,2,3}$  are the three Pauli operators.

We perform a second transformation into a frame rotating with angular frequency  $\omega_p$  and use a RWA to compute the eigenenergies of Equation 6.8. For large values of  $\Omega'$  the energies take the values  $E_{\uparrow,\downarrow} \approx \pm\Omega'/2 + (\Delta')^2/2\Omega'$ . Even though  $E_{\uparrow,\downarrow}$  are still first order sensitive to  $\Omega$  because  $\Delta' \approx \omega_{z,x} \propto \Omega$ , its effect is suppressed by a factor of  $1/\Omega'$ . Thus, the concatenated CDD field protects from the fluctua-

tions  $\delta\Delta'$  of the first dressing field in a similar way that CDD provided protection from detuning noise  $\delta\Delta$ . Table 6.1 summarizes the dependence of the  $|xyz\rangle$  and  $|\uparrow\downarrow\rangle$  energies on  $\Delta$ ,  $\Omega$  and  $\Omega'$ .

Table 6.1: Energies of the CDD and CCDD states as a function of  $\Delta$ ,  $\Omega$  and  $\Omega'$ . The dependence on parameters not relevant to the expansion is given by the functions  $f_1$ ,  $f_2$ ,  $g_1$  and  $g_2$ .

|                              | CDD  | concatenated CDD  |
|------------------------------|--|---|
| $\Delta$ dependence          | $f_1(\epsilon, \Omega)\Delta^2$                  | $f_2(\Omega, \epsilon)\frac{\Delta^2}{\Omega'}$   |
| $\Omega, \Omega'$ dependence | $\Omega + g_1(\Delta, \epsilon)\frac{1}{\Omega}$ | $\left[\Omega^2 + \epsilon\Omega + g_2(\Delta, \epsilon)\frac{1}{\Omega}\right]\frac{1}{\Omega'}$ |

We produced doubly-dressed states by doing (one more!) ARP sequence. We initialized the system in the  $|\downarrow\rangle$  state with RF coupling strength  $\Omega_i$ . We set the probe frequency to be  $\sim 20$  kHz off resonant with respect to the  $|\downarrow\rangle \rightarrow |\uparrow\rangle$  transition and ramped it on in 10 ms. We then ramped  $\Omega_i \rightarrow \Omega_f$  in 30 ms. The experimental sequence can be visualized in Figure 10. We chose the value of  $\Omega_f$  such that it would bring  $\omega_p$  to resonance at  $\Delta = 0$ , creating double dressed states that were equal superposition of  $|\downarrow\rangle$  and  $|\uparrow\rangle$ . We quantified the sensitivity of this transition to large changes in the detuning  $\Delta$  in terms of the fractional population imbalance  $\langle\hat{\sigma}_3\rangle = P_\downarrow(\Delta) - P_\uparrow(\Delta)$ , shown in Figure 11a for  $\Omega_f/2\pi = 138.2(1)$  kHz <sup>4</sup>. This signal is first-order sensitive to  $\omega_{\downarrow,\uparrow}$ , and provided our third measurement of sensitivity to detuning in Figure 6b denoted by circles.

We compared the fidelity of preparing a superposition of the  $|\downarrow\rangle$  and  $|\uparrow\rangle$

---

<sup>4</sup>We chose the maximum value of  $\Delta$  such that the population of  $|y\rangle$ , was negligible after de-loading.

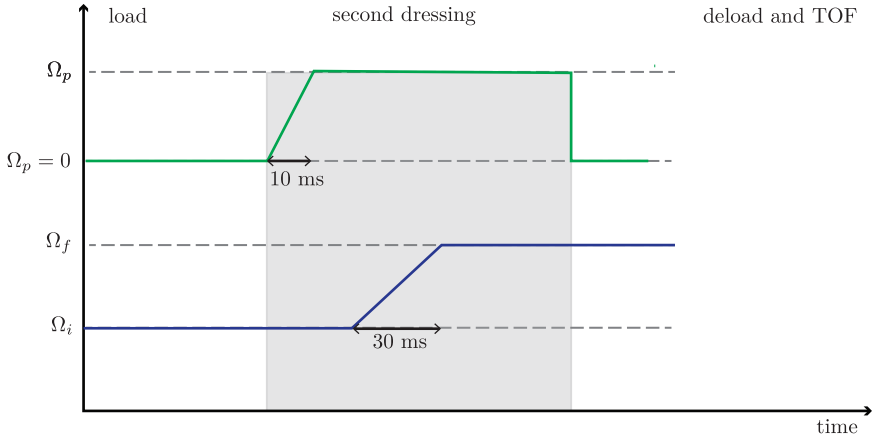


Figure 10: Experimental protocol for implementing concatenated CDD. We started an initial RF coupling strength  $\Omega_i$  and ramped on the probe field  $\Omega_p$  in a few ms with  $\omega_p = \omega_{z,x}(\Omega_f)$  so that it was initially slightly off resonant with the  $zx$  transition. We then ramped the RF field to  $\Omega_f$ , bringing  $\omega_p$  to resonance.

states to adiabatically preparing a similar superposition of the the  $|m_F = 0\rangle$  and  $|m_F = -1\rangle$  states using a single ARP (no dressed states involved), both with a probe field strength of  $\approx 1$  kHz. Figure 11b shows the RMS deviation of the population imbalance measured over a few hundred repetitions of the experiment. The RMS deviation for the dressed basis is  $0.024(1)$  and is an order of magnitude smaller than for the  $|m_F\rangle$  basis  $0.29(1)$ , where it practically impossible to prepare a balanced superposition for the parameters used here <sup>5</sup>.

Figure 11c shows the response of the  $|\downarrow\rangle \rightarrow |\uparrow\rangle$  transition to small changes  $\delta\Omega$  for different values of  $\Omega_p$ . We prepared an equal superposition of  $|\downarrow\rangle$  and  $|\uparrow\rangle$  following the same procedure as before for  $\Omega_f/2\pi = 138.2(1)$  kHz. We then measured how the population imbalance changes for small variations of  $\Omega$  — the effective detuning in the ‘twice-rotated frame’ — for different probe amplitudes  $\Omega_p$ . We

---

<sup>5</sup>In Figure 11b, the noise in the  $|m_F\rangle$  basis is not Gaussian distributed as is typical of line noise in these experiments.

defined a sensitivity parameter  $d\langle\hat{\sigma}_3\rangle/d\Omega$ , obtained from the linear regime of the population imbalance measurements (see inset in Figure 11c). The robustness of the doubly-dressed states against  $\delta\Omega$  fluctuations increased with  $\Omega_p$ , thus verifying the concatenating effect of CDD in the  $|xyz\rangle$  basis.

However promising the application of multiple concatenating fields might seem, this procedure has a fundamental limitation. Each time a new coupling field is applied the energies of the dressed states are reduced to something on the order of magnitude of the coupling strength from the applied concatenating field. For example, in the experiments we described here we started with  $|m_F\rangle$  states with transition frequencies on the order of MHz. The transition frequencies of the  $|xyz\rangle$  states were reduced to hundreds of kHz (or in general the magnitude of  $\Omega$ ). After applying the second concatenating RF field the transition frequencies of the  $|\Downarrow\uparrow\rangle$  are of the order of  $\Omega_p \sim 10$  kHz which needs to be smaller than  $\Omega$  for the second RWA to be valid. Therefore we see that after applying multiple concatenating fields we are at the risk of having some very robust states that are also very closely spaced in energy which might not be desirable for some applications.

## 6.10 Conclusions

We realized a three-level system that is dynamically decoupled from low-frequency noise in magnetic fields, measured now-allowed transitions between all three states, and demonstrated control techniques for creating arbitrary Hamiltonians. These techniques add no heating or loss mechanisms, yet within the protected

subspace retain the full complement of cold-atom coherent control tools such as optical lattices and Raman laser coupling, and permit new first-order transitions that are absent in the unprotected subspace. These transitions enable experiments requiring a fully connected geometry as for engineering exotic states, e.g., in cold-atom topological insulators, and two-dimensional Rashba spin-orbit coupling in ultracold atomic systems [22, 98].

The synthetic clock states form a decoherence-free subspace that can be used in quantum information tasks where conventional clock states might be absent, or incompatible with other technical requirements [99]. Moreover, their energy differences are proportional to the amplitude of the dressing field, and hence tunable, so they can be brought to resonance with a separate quantum system. The effective quantization axis can be arbitrarily rotated so that the two systems can be strongly coupled, pointing to applications in hybrid quantum systems [100, 101]. Introducing a second coupling field shields the system from fluctuations of the first, a process that can be concatenated as needed. More broadly, synthetic clock states should prove generally useful in any situation where fluctuations of the coupling field can be made smaller than those of the environment.

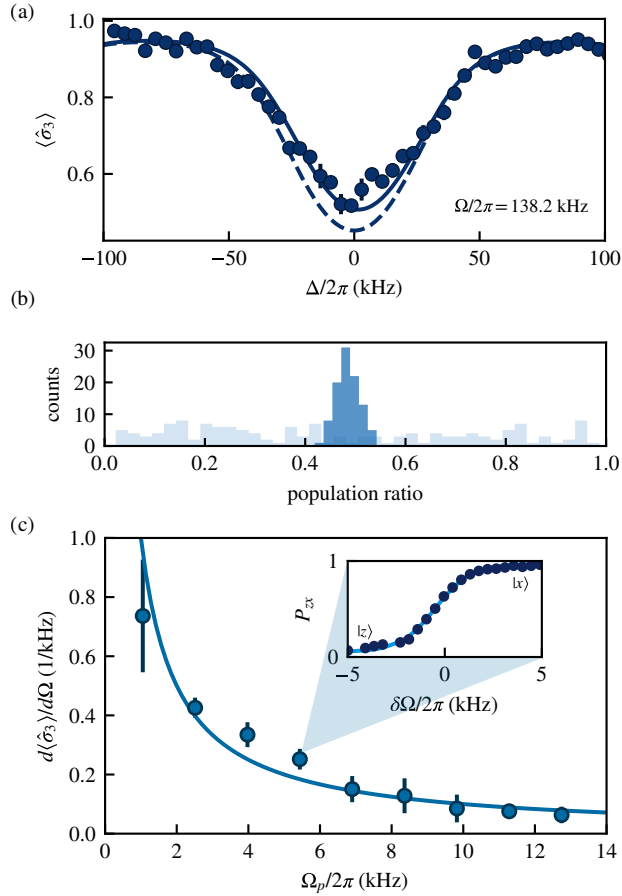


Figure 11: (a) The fractional population imbalance of the  $\downarrow\uparrow$  transition for  $\Omega/2\pi = 138.2(1)$  kHz over detuning  $\Delta$ . The dashed curve is calculated using Equation 6.7 and the solid one using the full Breit-Rabi expression. (b) The fidelity of preparing a balanced superposition of  $|\downarrow\rangle$  and  $|\uparrow\rangle$  (dark blue) states compared to  $|m_F = 0\rangle$  and  $|m_F = -1\rangle$  states (light blue). (c) The robustness of  $\downarrow, \uparrow$  transition against fluctuations  $\delta\Omega$  for different probe field coupling strengths. The points represent the slope of the fitted curves to the fractional population imbalance (inset).

## Chapter 7: Topological order in quantum systems

Topological order can be found in a wide range of physical systems, from crystalline solids [20], photonic meta-materials [102] and even atmospheric waves [103] to optomechanic [104], acoustic [105] and atomic systems [106]. Topological systems are a robust foundation for creating quantized channels for transporting electrical current, light, and atmospheric disturbances. These topological effects can be quantified in terms of integer-valued invariants such as the Chern number, applicable to the quantum Hall effect [107, 108], or the  $\mathbb{Z}_2$  invariant suitable for topological insulators [109].

The topology of Bloch bands defines integers that serve to both classify crystalline materials and precisely specify properties, such as conductivity, that are independent of small changes to lattice parameters [20]. Topologically non-trivial materials first found application in metrology with the definition of the von Klitzing constant as a standard of resistance, which is now applied in the realization of the kilogram [110]. Today, topological systems have found applications in the engineering of low loss optical waveguides [102] and present a promising path to quantum computation [111].

We got interested in topology when working on a system with Rashba [21]

type spin-orbit coupling in the lab. Our system had non-trivial topology but it broke from the usual mold of topological materials as it didn't have an underlying crystalline structure that conventionally yields to integer Chern numbers.

Before describing our experiments to both engineer and characterize the unconventional topology of a Rashba spin-orbit coupled gas, in this Chapter I take a step back to describe the basic concepts of topology and its applications to the band theory of solids. The ideas of topology and how exactly one can connect donuts with band structures might feel a bit obscure and complicated for non-experts in the field. ~~I wrote this Chapter with that in mind, with the hope that it can be followed by non-experts and provide some insight and intuition about this field.~~ The concepts introduced in this Chapter will be necessary for understanding the results presented in Chapter 8.

## 7.1 Topology in mathematics

Topology is a branch of mathematics that studies continuity [112]. The most familiar example might be that of objects being continuously deformed into one another. For example, a donut can be continuously deformed into a coffee mug but if we want to deform it into a pretzel we need to poke more holes in it. This gives us some intuition that the donut and the mug must share the same topology, which is different from that of the pretzel. Topology also studies more abstract objects but I will limit the discussion to closed two-dimensional surfaces (manifolds) in three dimensions, which will be enough to provide some intuition when we define

topological invariants for band structures in the following sections.

The topology of 2D surfaces can be classified by the Euler characteristic, and it is related to the local Gaussian curvature of a surface by the Gauss-Bonet theorem. The Gaussian curvature can be interpreted in the following way: at any point  $\mathbf{x}_0$  on a surface we can find a normal vector  $\hat{n}$  that is orthogonal to the tangent plane of the surface (red arrow in Figure 1). We can then define a family of planes containing  $\hat{n}$  and the intersection between any of these planes and the surface defines a curve. If we perform a Taylor expansion of the curve around  $\mathbf{x}_0$  the quadratic term defines what is known as the normal curvature  $\kappa$ . The orange and blue lines in Figure 1 are two examples of such curves and their curvatures correspond to the minimum and maximum value of the surface; they are what is known as the principal curvatures  $\kappa_{min}$  and  $\kappa_{max}$ . The Gaussian curvature at any point of a surface is defined in terms of the principal curvatures as  $K = \kappa_{min}\kappa_{max}$  [112].

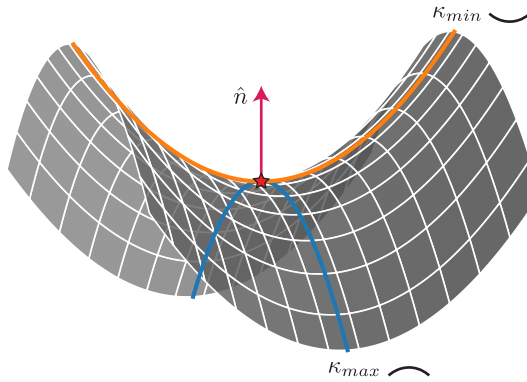


Figure 1: The intersection of planes containing the normal vector  $\hat{n}$  at  $\mathbf{x}_0$  (red star) and the gray surface define a family of curves. The minimum and maximum curvatures, corresponding to the orange and blue lines respectively, correspond to the principal curvatures of the surface at  $\mathbf{x}_0$ .

The Gauss-Bonnet theorem states that the integral of the local Gaussian curvature over a closed surface is equal to the integer valued Euler characteristic

$$\chi = \frac{1}{2\pi} \int_S K dA, \quad (7.1)$$

which is related to the genus  $g$  (number of holes or handles in the surface) by  $\chi = 2(1 - g)$ . The Gauss-Bonnet theorem is a very powerful result as it relates the local properties of a surface, the Gaussian curvature, with a global topological invariant, the Euler characteristic.

In the following sections I will introduce topological invariants in the context of condensed matter physics, which even though might seem a bit more abstract, their interpretation can be closely related to the concepts just defined in this section.

## 7.2 Topological order in condensed matter

Just like topology classifies properties of geometric objects, one important task of condensed matter physics has been to classify phases of matter. Many of these phases, for example, magnetic or conducting phases, can be described in terms of order parameters related to spontaneously broken symmetries [113]. However, in the past few decades, an increasing number of systems have been found where it is only possible to understand their phases and properties in terms of the underlying topology of their quantum states. This new paradigm of physics has been so important that in 2016 the Nobel prize in physics was awarded to David J. Thouless, F. Duncan M. Haldane and J. Michael Kosterlitz for the theoretical discoveries of

The effects of topology in condensed matter systems were first observed when von Klitzing and colleagues [114] measured the quantized Hall resistance in two-dimensional electron gases subjected to a strong perpendicular magnetic field. The effect can be understood semi-classically by thinking of the electrons' quantized cyclotron orbits<sup>1</sup> that give rise to Landau levels. If the Landau levels are filled then there is an energy gap separating two consecutive levels and the material acts as an insulator but if an electric field is applied the orbits drift and the electrons will be 'skipping orbits' in the edge as can be seen in Figure 2, giving rise to what is known as edge states.

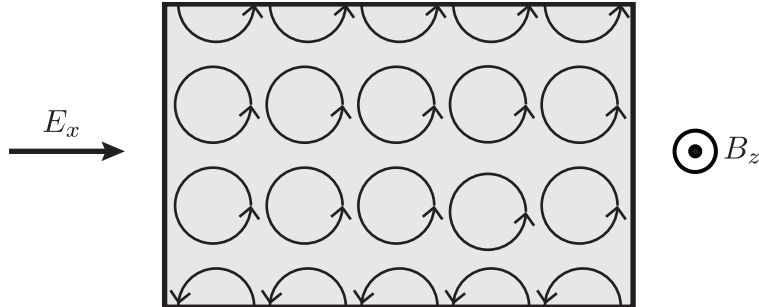


Figure 2: The quantum Hall effect. An electron gas is confined in a two-dimensional material and a strong magnetic field is applied perpendicular to the plane. The electrons on the bulk travel in cyclotron orbits while the electrons on the edge travel 'skipping orbits'.

In a seminal paper Thouless, Kohomoto, Nightingale, and den Nijs [107] explained that the quantization of the Hall conductivity is determined by the under-

---

<sup>1</sup>This is an intuitive but not very complete explanation of the quantum Hall effect, see [115] if you want to learn more about this subject.

lying topology of the band structure. Just like the Euler characteristic defined in Equation 7.1 classifies 2D solids that can be continuously deformed without opening or closing holes, there is a topological invariant that classifies band structures that can be deformed into one another without opening or closing an energy gap. This invariant, initially known as the ‘TKNN invariant’, was later recognized by the mathematical physicist Barry Simon as the ‘first Chern class invariant from  $U(1)$  fiber bundles’<sup>2</sup> [117] and the TKNN invariant became what is known today as the Chern number or Chern invariant. Another very valuable contribution from Simon’s work was that he made the connection between the Chern number and the Berry’s geometrical phase [118] which will be defined in the following sections and will allow us to make a physical interpretation of this otherwise abstract seeming topological invariant.

### 7.3 Berry phase and Berry curvature

A Berry or geometric phase is used to describe the phase acquired by a quantum state as it moves through a closed trajectory in parameter space. It plays a key role in topological band theory and can help provide a physical interpretation of the Chern number.

Consider a Hamiltonian  $\hat{H}$  that depends on a set of parameters  $\mathbf{r} = (r_1, r_2, \dots)$ . If the parameters are slowly changed in time, the corresponding change in the system can be described by a path in parameter space  $\mathbf{r}(t)$ . The state  $|\psi(t)\rangle$  evolves

---

<sup>2</sup>See [116] if you want to dive into hardcore topology.

according to the time dependent Schrödinger equation and at any given time  $t$  there is a basis that satisfies

$$\hat{H}(\mathbf{r}) |n(\mathbf{r})\rangle = E_n(\mathbf{r}) |n(\mathbf{r})\rangle \quad (7.2)$$

for  $\mathbf{r} = \mathbf{r}(t)$ . Suppose the system is initially in state  $|n(\mathbf{r}(t=0))\rangle$ , if the parameters are changed slowly such that the adiabatic theorem is valid, then at time  $t$  the state of the system can be written as

$$|\psi(t)\rangle = \exp \left\{ -\frac{i}{\hbar} \int_0^t dt' E_n(\mathbf{r}(t')) \right\} \exp(i\gamma_n(t)) |n(\mathbf{r}(t))\rangle, \quad (7.3)$$

where the first exponential term corresponds to a dynamical phase factor, and the second term is a geometric phase. By imposing that  $|\psi(t)\rangle$  satisfies the time-dependent Schrödinger equation one finds that

$$\gamma_n(t) = i\langle n(\mathbf{r}) | \nabla_{\mathbf{r}} n(\mathbf{r}) \rangle \cdot \dot{\mathbf{r}}(t), \quad (7.4)$$

where the term

$$\mathbf{A}_n(\mathbf{r}) = i\langle n(\mathbf{r}) | \nabla_{\mathbf{r}} n(\mathbf{r}) \rangle \quad (7.5)$$

is usually referred to as the Berry connection<sup>3</sup> or the Berry vector potential for reasons that will become apparent. Because eigenvectors can only be defined up to a global phase,  $\mathbf{A}$  is a gauge dependent quantity. If we make a gauge transformation such that  $|n(\mathbf{k})\rangle \rightarrow e^{i\xi(\mathbf{k})} |n(\mathbf{k})\rangle$  then the Berry connection is also transformed as

---

<sup>3</sup>This is related to the connection defined in differential geometry that is used to describe things like parallel transport.

$\mathbf{A}_n(\mathbf{k}) \rightarrow \mathbf{A}_n(\mathbf{k}) - \nabla_{\mathbf{k}}\xi(\mathbf{k})$ . However if we integrate the Berry connection on a closed loop

$$\gamma_n(\mathcal{C}) = \oint_{\mathcal{C}} \mathbf{A}_n(\mathbf{r}) \cdot d\mathbf{l}, \quad (7.6)$$

we obtain the Berry phase which, unlike the Berry connection, is gauge independent (modulo  $2\pi$ ).

An alternative way to compute Berry's phase uses Stokes's theorem from vector calculus

$$\begin{aligned} \oint_{\mathcal{C}} \mathbf{A}_n \cdot d\mathbf{l} &= \int_{\mathcal{S}} \nabla \times \mathbf{A}_n \cdot d\mathbf{S} \\ &= \int_{\mathcal{S}} \boldsymbol{\Omega}_n \cdot d\mathbf{S}, \end{aligned} \quad (7.7)$$

where the vector field  $\boldsymbol{\Omega}_n = \nabla \times \mathbf{A}_n$  is known as the Berry curvature or Berry field. By rewriting the Berry phase in this way, its resemblance with the definition of the Euler characteristic from Equation 7.1 becomes apparent.

Using some vector calculus identities the Berry curvature can be rewritten as

$$\begin{aligned} \boldsymbol{\Omega}_n &= i[\nabla_{\mathbf{r}} \langle n |] \times [\nabla_{\mathbf{r}} |n \rangle] \\ &= \sum_{j \neq n} i[\langle n | \nabla_{\mathbf{r}} |j \rangle] \times [\langle j | \nabla_{\mathbf{r}} |n \rangle] \\ &= i \sum_{j \neq n} \frac{\langle n | \nabla_{\mathbf{r}} \hat{H} |j \rangle \times \langle j | \nabla_{\mathbf{r}} \hat{H} |n \rangle}{(E_j - E_n)^2}, \end{aligned} \quad (7.8)$$

where  $\langle n | \nabla_{\mathbf{r}} |j \rangle$  was replaced with  $\langle n | \nabla_{\mathbf{r}} \hat{H} |j \rangle / (E_j - E_n)$  by differentiating Equa-

tion 7.2. This expression shows that  $\Omega_n$  is a gauge independent quantity as it does not depend on the derivatives of a particular gauge choice for  $|n\rangle$  but rather on  $\nabla_{\mathbf{r}}\hat{H}$  which is gauge independent. Also we can see that  $\Omega_n$  becomes singular when there are degeneracies present in the Hamiltonian, and these degeneracies act as ‘sources’ for the Berry curvature. Finally, even though the system may remain in state  $|n\rangle$  during the adiabatic evolution, this expression for the Berry curvature makes it explicit that other eigenstates of the Hamiltonian have an influence in the Berry phase acquired.

### 7.3.1 Aharonov-Bohm phase as an example of a Berry’s phase

A familiar example of geometric phases is the Aharonov-Bohm phase [119] gained by an electron moving along closed trajectories around a solenoid. This phase was initially conceived as a way of showing that in quantum mechanics magnetic vector potentials, typically conceived only as mathematical objects, can have a physical effect on the wave function. They considered a coherent electron beam split into two paths around a solenoid that produces a magnetic field  $\mathbf{B}$  and later recombined as shown in Figure 3. Outside the solenoid the magnetic field  $\mathbf{B} = 0$ , but there can be a non-zero magnetic vector potential such that  $\mathbf{B} = \nabla \times \mathbf{A}$ . Even though the electron’s trajectories are not modified by the presence of the solenoid, when looking at the interference pattern one finds that the two paths acquired different phases, and their difference is remarkably equal to magnetic flux piercing the area enclosed by the path of the electrons  $\Delta\varphi = 2\pi\Phi_B/\Phi_0$ , where  $\Phi_0 = h/e$  is the

flux quantum. This Aharonov-Bohm phase can be interpreted as an example of a Berry phase in real space.

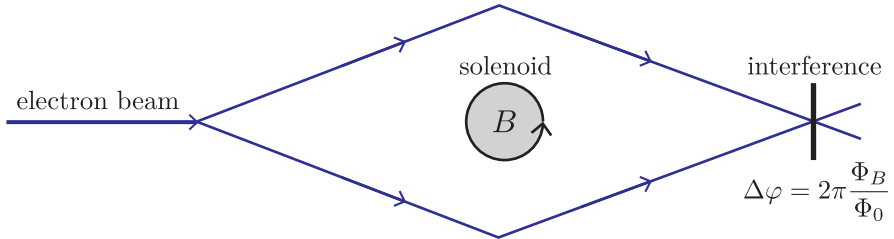


Figure 3: The Aharonov-Bohm experiment. A coherent electron beam is split into two paths surrounding a solenoid which produces a non-zero magnetic field  $\mathbf{B}$  inside the gray region and  $\mathbf{B} = 0$  outside. The two beams are later recombined and an interference pattern reveals a phase difference  $\Delta\varphi = 2\pi\Phi_B/\Phi_0$  equal to the magnetic flux enclosed by the electron's path.

For a charged particle in the presence of a vector potential, the momentum dependence of the free-particle Hamiltonian is modified  $\mathbf{p} \rightarrow \mathbf{p} - q\mathbf{A}$  so that the wave function will depend on the magnetic vector potential as well. Using Equations 7.6 and 7.7 it can be shown that the Berry phase associated with a closed path around the solenoid is exactly equal to the Aharonov-Bohm phase:

$$\begin{aligned}\gamma_n(\mathcal{C}) &= \frac{e}{\hbar} \oint_C \mathbf{A}(\mathbf{r}) \cdot d\mathbf{r} \\ &= \frac{e}{\hbar} \int_S \nabla \times \mathbf{A} \cdot d\mathbf{S} \\ &= \frac{e\Phi_B}{\hbar},\end{aligned}\tag{7.9}$$

In this particular example, the Berry connection is exactly equal to the magnetic vector potential and the Berry curvature is the magnetic field. This gives us a very physical intuition for interpreting the Berry phase in terms of the ‘magnetic

flux' from abstract sources of 'magnetic fields' in parameter space.

### 7.3.2 Chern number

The Chern number is conventionally used to describe the topology of materials which have an underlying crystalline structure. According to Bloch's theorem, the wave functions of a space periodic Hamiltonian can be written as  $|\psi(\mathbf{k})\rangle = e^{i\mathbf{k}\cdot\mathbf{r}}|u(\mathbf{k})\rangle$ <sup>4</sup>, where  $\mathbf{r}$  is the position and  $\mathbf{k}$  the crystal momentum. The wave functions  $|u(\mathbf{k})\rangle$  are periodic and therefore invariant under the displacement operator  $\hat{D}(n d)|u(\mathbf{k})\rangle = |u(\mathbf{k})\rangle$  when  $d$  is the unit cell size and  $n$  an integer. If we define the Bloch Hamiltonian

$$\hat{H}(\mathbf{k}) = e^{i\mathbf{k}\cdot\mathbf{r}}\hat{H}e^{-i\mathbf{k}\cdot\mathbf{r}}, \quad (7.10)$$

their eigenvectors are given by  $|u(\mathbf{k})\rangle$  and the eigenvalues define the band structure. Translational symmetry implies that  $\hat{H}(\mathbf{k} + \mathbf{a}) = \hat{H}(\mathbf{k})$  where  $\mathbf{a}$  is a reciprocal lattice vector. The crystal momentum or quasimomentum (in analogy to the Floquet quasienergy) is only defined within the periodic Brillouin zone and therefore can be mapped into a torus in  $d$  dimensions if we glue the edges together.

The Chern number of the  $n$ th band is defined as

$$C_n = \frac{1}{2\pi} \int_{BZ} \boldsymbol{\Omega}_n \cdot d\mathbf{k}, \quad (7.11)$$

where the relevant parameter space is crystal momentum and the surface of integration

---

<sup>4</sup>Very much like Floquet theory in momentum space

tion corresponds to the BZ (a torus). The definition of the Chern number is closely related to the Berry phase from Equation 7.7. For our previous example of a quantum Hall system, the integer proportionality factor in the quantized conductance is exactly equal to the Chern number.

Just like two-dimensional surfaces are classified by the integral of their Gaussian curvature, the topology of Bloch bands and quantum systems, in general, is determined by the integral of the Berry curvature. Similarly, the integral connects local properties of a quantum system, the Berry connection, with a global topological invariant, the Chern number. One subtle difference is that the Euler characteristic is only determined by the surface (and its intrinsic Gaussian curvature) while the Chern number is defined both by a surface (the BZ) and an additional local curvature (the Berry curvature). By considering different lattice Hamiltonians one can obtain a different Berry curvature, but the geometry of the BZ and thereby the surface of integration is typically defined by a torus<sup>5</sup>. This difference will be important later on when we describe the experiments performed to study a system with Rashba spin-orbit coupling where the unit cell size is taken to infinity (i.e. we remove the lattice).

## 7.4 The bulk-edge correspondence principle

Earlier I mentioned that topological systems provide very robust channels for transporting things like electrical current and light. Transport phenomena typically

---

<sup>5</sup>In the next chapter we consider a case where this breaks down.

arise when there is a spatial interface between two topologically distinct phases. The electrons skipping orbits at the interface of a (topological) quantum Hall material and (trivial) vacuum are one example of this. Notice that for this particular example the modes propagate along a given direction, they are chiral. In general, one can expect to have modes moving along two directions, and the difference between the number of these modes  $N_L - N_R$  is fixed and determined by the topology of the bulk states. The bulk-edge correspondence principle relates the difference in the number of these modes with the bulk topology of the materials at the interface:

$$\Delta C = N_R - N_L \quad (7.12)$$

where  $\Delta C$  is the difference of Chern number on the interface.

## 7.5 Example: two-level model

Many of the concepts introduced in the previous section can be readily applied and understood using a two-level model

$$\hat{H}(\mathbf{k}) = \mathbf{h}(\mathbf{k}) \cdot \hat{\boldsymbol{\sigma}} \quad (7.13)$$

where  $\hat{\boldsymbol{\sigma}} = (\sigma_x, \sigma_y, \sigma_z)$  are the Pauli matrices and  $\mathbf{h}(\mathbf{k}) = (h_x(\mathbf{k}), h_y(\mathbf{k}), h_z(\mathbf{k}))$  are functions of  $\mathbf{k}$ . This model has been used to describe a number of physical systems like graphene [108] and spin-orbit coupled systems [21, 48]. Let us now consider the simple case  $h(\mathbf{k}) = \mathbf{k}$ , for which  $\nabla_{\mathbf{k}} \hat{H} = \boldsymbol{\sigma}$  and using Equation 7.8 it can be shown

that

$$\Omega = -\frac{\mathbf{h}}{2h^3} \quad (7.14)$$

which can be recognized as the field of a Dirac monopole [120] with charge  $-1/2$ . The degeneracy in the energies that gives rise to the monopole is known as a Dirac point as the energies in that vicinity resemble the dispersion of a massless Dirac particle. In 2D materials where  $\mathbf{k}$  is only defined within 2D plane  $h_z$  corresponds to the mass of a Dirac particle but its effect on the Berry curvature is equivalent to that of moving the Dirac monopole along a fictitious  $k_z$  dimension in a direction determined by the sign of  $h_z$ .

It follows from Equation 7.14 that the Berry phase gained by moving along a closed path  $\mathcal{C}$  is equal to the flux from the monopole in the surface enclosed by  $\mathcal{C}$  as is shown in Figure 4. This connects nicely with our intuition from the Aharonov-Bohm effect. For a closed surface enclosing the Dirac point, the Chern number is an integer equal to 1.

For a Hamiltonian with arbitrary  $\mathbf{h}(\mathbf{k})$  we can define a normalized vector  $\hat{h} = \mathbf{h}/|\mathbf{h}|$  and the Chern number takes the form

$$C = \frac{1}{4\pi} \int (\partial_{k_x} \hat{h} \times \partial_{k_y} \hat{h}) \cdot \hat{h} d^2k \quad (7.15)$$

which can be interpreted as the number of times that the vector  $\hat{h}(\mathbf{k})$  wraps around a unit sphere [121], a quantity that is known as the winding number. Depending on the sign of  $h_z$  the vector  $\hat{h}(\mathbf{k})$  will wrap around the north or south hemisphere,

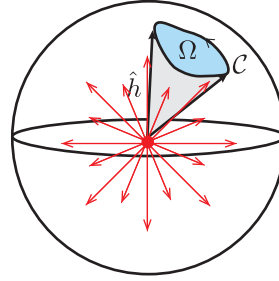


Figure 4: For a two-level system, the Berry curvature from a Dirac point can be viewed as a Dirac monopole in momentum (parameter) space. The Chern number can be interpreted as the flux from the monopole on the solid angle subtended by the vector  $\hat{h}(\mathbf{k})$  or alternatively as the number of times  $\hat{h}(\mathbf{k})$  wraps around a unit sphere.

so to have integer valued Chern numbers, Dirac points must come in pairs. Luckily for lattice Hamiltonians this is guaranteed by the fermion doubling theorem [122]. In Chapter 8 I describe an engineered system that has a single Dirac point.

## 7.6 Monopoles and Dirac strings

We just gained some intuition about interpreting the Chern number as the flux from Dirac monopoles. But if we stick to our knowledge of electromagnetism we might remember that magnetic monopoles are forbidden since

$$\nabla \cdot \mathbf{B} = \nabla \cdot (\nabla \times \mathbf{A}) = 0. \quad (7.16)$$

So how is it possible to keep a vector potential and have  $\nabla \cdot \mathbf{B} \neq 0$ ? The solution to this problem was envisioned by Dirac [120] and is now called a Dirac string. If we consider a semi-infinitely long and infinitesimally thin solenoid, the magnetic field

in the finite end will resemble that of a monopole as can be seen in Figure 5. This tiny solenoid corresponds to the Dirac string. A more mathematical interpretation

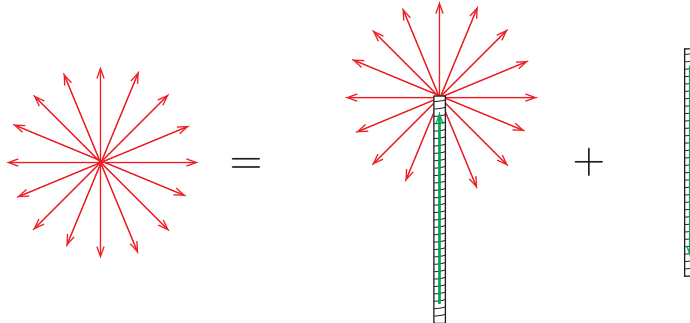


Figure 5: For a two-level system, the Berry curvature from a Dirac point can be viewed as a Dirac monopole in momentum (parameter) space. The Chern number can be interpreted as the flux from the monopole on the solid angle subtended by the vector  $\hat{h}(\mathbf{k})$  or alternatively as the number of times  $\hat{h}(\mathbf{k})$  wraps around a unit sphere.

of these strings comes from the fact that in order to have  $\nabla \cdot \mathbf{B} \neq 0$  the vector potential of a monopole must have ‘lines’ where it becomes singular. For example, we can write for a particular gauge

$$\mathbf{A}(\mathbf{r}) = g \frac{-y\mathbf{e}_x + x\mathbf{e}_y}{r(r+z)} \quad (7.17)$$

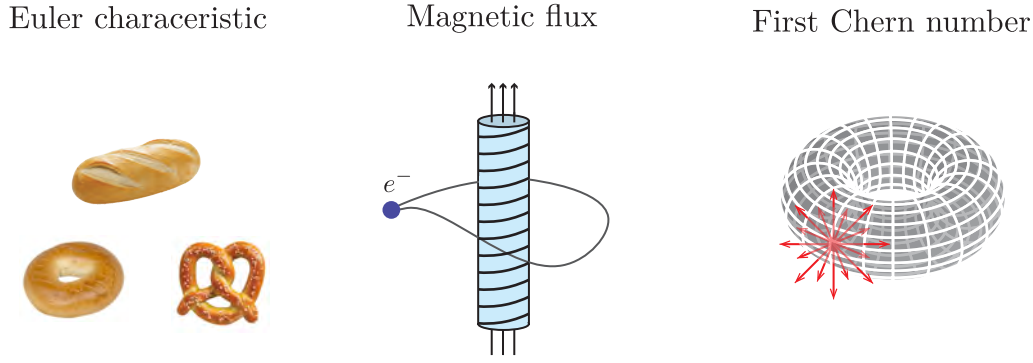
which is singular at the Dirac string located at the negative  $z$  axis where  $z = -r$ . The orientation of the Dirac string is gauge dependent, something that should not surprise or bother us at this point. However, the physical effects of the Dirac string should be gauge independent, or in other words, the Aharonov-Bohm phase gained by a charged particle moving in a path that encloses the string should be an integer multiple of  $2\pi$ . This argument gives rise to the Dirac charge quantization [120],

and in the context of topology, it guarantees that when we calculate the Berry phase by integrating the Berry connection (vector potential) along a path that encloses a Dirac string, its effect will be indistinguishable.

## 7.7 Conclusions

Topology plays a very important role both in [math](#) and in physics. In this Chapter I reviewed the basic concepts of topology in the context of condensed matter physics that will be relevant for our experiments with unconventional topology.

As a closing remark, Figure 6 summarizes the main concepts that were introduced and is a reminder that topological invariants are global properties defined in terms of integrals of local properties. Furthermore, we can use our intuition from electromagnetic theory to interpret topological invariants in quantum mechanics.



$$\chi = \frac{1}{2\pi} \int_{\mathcal{M}} K dS \quad \Phi = \int_{\mathcal{S}} \mathbf{B} \cdot d\mathbf{S} \quad C_n = \frac{1}{2\pi} \int_{BZ} \boldsymbol{\Omega}_n \cdot d\mathbf{k}$$

Figure 6: The Euler characteristic and the Chern number are topological invariants defined by integrals of local curvatures. The Aharonov-Bohm phase gives us physical intuition to interpret the Chern number as the flux from a ‘Berry field’.